

Topological flat bands in a kagomé lattice multiorbital system*

Satoshi Okamoto,^{1,†} Narayan Mohanta,¹ Elbio Dagotto,^{1,2} and D. N. Sheng³

¹*Materials Science and Technology Division, Oak Ridge National Laboratory, Oak Ridge, Tennessee 37831, USA*

²*Department of Physics and Astronomy, The University of Tennessee, Knoxville, Tennessee 37996, USA*

³*Department of Physics and Astronomy, California State University, Northridge, California 91330, USA*

Flat bands and dispersive Dirac bands are known to coexist in the electronic bands in a two-dimensional kagomé lattice. With the relativistic spin-orbit coupling, such systems often exhibit nontrivial band topology, allowing gapless edge modes between flat bands and dispersive bands or at the Dirac band crossing. Here, we theoretically demonstrate that a multiorbital system on a kagomé lattice is a versatile platform to explore the interplay between interaction and nontrivial band topology. When a flat band is 1/3 filled, non-local repulsive interactions further induce a fractional quantum Hall state. We also discuss the possible realization of our findings in real kagomé materials.

Introduction.— Flat-band systems have been proposed as ingenious theoretical models to prove the existence of ferromagnetic ordering with itinerant electrons [1–4]. Theoretical developments in such flat-band systems have been made almost in parallel with those in so-called topological insulators (TIs) [5–8]. Nontrivial topology of electronic bands in a kagomé lattice, one of flat-band systems, has been extensively studied [9–18].

Experimental quests of topological materials with kagomé lattice have also been carried out. Many of such experimental efforts were stimulated by the prediction of Weyl semimetals [19, 20], including intermetallic compounds involving Co [21–25], Fe [26–29], and Mn [30–32], and van-der-Waals compounds [33], as well as optical lattices [34, 35]. More recently, the coexistence of superconductivity and nontrivial band topology was reported in a kagomé compound [36–39].

When a flat band is partially occupied by electrons, Coulomb repulsive interactions could become dominant over electronic kinetic energy. This situation is already realized in two-dimensional electron gases under applied magnetic fields, where flat bands correspond to Landau levels. Fractional quantum Hall (FQH) effects were thus discovered [40, 41]. An exact numerical analysis made an important contribution by demonstrating that full quantum fluctuations are essential to stabilize FQH states over charge density wave states [42]. Once charge excitation gap is induced at fractional filling, the property of FQH states is elegantly explained using effective theory [43].

Recently, further intriguing proposals were put forward

by considering flat bands with nontrivial topology and repulsive interactions, whereby FQH states could be generated without having Landau levels. These proposals considered single-band models on a kagomé lattice [44, 45], checkerboard lattices [46–50], a Haldane model on a honeycomb lattice and a ruby lattice [45], as well as multi-band models on a buckled honeycomb lattice [51], a triangular lattice [52], and a square lattice for the mercury-telluride TI [45]. It was later revealed that quantum Hall states realized in flat band systems and those realized under an applied magnetic field are adiabatically connected [53]. When realized in real materials, FQH states in flat band systems would become a vital element of topological quantum computing [54, 55]. Based on the numerical results [44–52], the possibility of FQH states was suggested in some of flat band systems [12, 15, 17]. However, the material realization of such FQH states has yet to be demonstrated as theoretical proposals often focus on one-band model and other proposed systems have small band gap.

Motivated by the recent experimental realization of kagomé materials, where multiple transition-metal d orbitals are active near the Fermi level, we consider in this work a multiorbital itinerant-electron model on a two-dimensional kagomé lattice. With the atomic spin-orbit coupling (SOC), this model shows multiple topological phases, including spin Hall insulators when spin splitting is absent and Chern insulators when spin splitting is induced. Interestingly, this model exhibit flat bands having nonzero Chern number as in a single-band kagomé system [10]. When such a flat band is fractionally occupied by electrons, non-local Coulomb interactions should induce FQH states. Our model calculation is particularly relevant to CoSn-type intermetallic compounds when a single kagomé layer becomes available.

Non-interacting model.—To begin with, we set up a multi-orbital tight-binding model on a kagomé lattice

$$H_t = - \sum_{\langle \mathbf{r} \mathbf{r}' \rangle} \sum_{\alpha \beta \sigma} \left(t_{\mathbf{r} \mathbf{r}'}^{\alpha \beta} c_{\mathbf{r} \alpha \sigma}^\dagger c_{\mathbf{r}' \beta \sigma} + \text{H.c.} \right), \quad (1)$$

as schematically shown in Fig. 1. Here, $c_{\mathbf{r} \alpha \sigma}^{(\dagger)}$ is the annihilation (creation) operator of an electron at site \mathbf{r} , orbital α with spin $\sigma = \uparrow$ or \downarrow . As discussed in Ref. [25],

* Copyright notice: This manuscript has been authored by UT-Battelle, LLC under Contract No. DE-AC05-00OR22725 with the U.S. Department of Energy. The United States Government retains and the publisher, by accepting the article for publication, acknowledges that the United States Government retains a non-exclusive, paid-up, irrevocable, world-wide license to publish or reproduce the published form of this manuscript, or allow others to do so, for United States Government purposes. The Department of Energy will provide public access to these results of federally sponsored research in accordance with the DOE Public Access Plan (<http://energy.gov/downloads/doe-public-access-plan>)

[†]okapon@ornl.gov

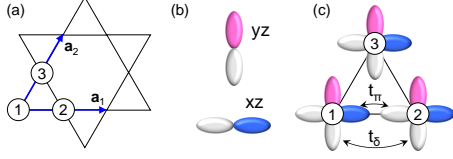


FIG. 1: Schematics of theoretical model. (a) Kagomé lattice with three sublattices, labeled 1, 2, and 3. Two arrows are lattice translation vectors $\mathbf{a}_{1,2}$. (b) Local orbitals $a = yz$ and $b = xz$. Colored ellipsoids indicate regions of electron wave functions, where the sign is positive. (c) Nearest-neighbor hopping integrals. $yz(xz)$ orbitals between site 1 and site 2 are hybridized via diagonal $t_{\delta(\pi)}$, i.e., $\delta(\pi)$ bonding. Other hopping integrals between site 2 and site 3 and between site 1 and site 3 are obtained by the Slater rule [56, 57].

CoSn-type kagomé systems have several flat bands with $\{yz, xz\}$, $\{xy, x^2 - y^2\}$, or $3z^3 - r^2$ character. We focus on a $\{yz, xz\}$ subset for simplicity and use $\alpha = a$ for yz orbital and b for xz orbital. With this basis, nearest-neighbor hopping integrals $t_{\mathbf{r}\mathbf{r}'}^{\alpha\beta}$ can be parameterized using Slater integrals [56]. Between site 1 and site 2, \hat{t}_{12} is diagonal in orbital indices as $t_{12}^{aa} = t_{\delta}$ and $t_{12}^{bb} = t_{\pi}$, corresponding to $(dd\delta)$ and $(dd\pi)$, respectively, in Ref. [56]. Other components are obtained by rotating basis a and b as shown in the supplementary information [57].

Since yz and xz are written using the eigenfunctions of angular momentum $l_z = \pm 1$ for $l = 2$ as $|yz\rangle = \frac{i}{\sqrt{2}}(|1\rangle + |-1\rangle)$ and $|xz\rangle = -\frac{1}{\sqrt{2}}(|1\rangle - |-1\rangle)$, respectively, the SOC $\lambda \vec{l} \cdot \vec{s}$ in the $\{yz, xz\}$ subset is written as

$$H_{soc} = \frac{\lambda}{2} \sum_{\mathbf{r}\sigma} \left(i\sigma_{\sigma\sigma}^z c_{\mathbf{r}a\sigma}^{\dagger} c_{\mathbf{r}b\sigma} + \text{H.c.} \right), \quad (2)$$

where $\hat{\sigma}^z$ is the z component of the Pauli matrices.

As shown in the supplementary information [57], an effective model for the $\{xy, x^2 - y^2\}$ doublet has the same form as the above $H_t + H_{soc}$. By symmetry, there is no hopping matrices between the $\{yz, xz\}$ doublet and other orbitals; xy , $x^2 - y^2$, and $3z^2 - r^2$, but the $\{xy, x^2 - y^2\}$ doublet and the $3z^2 - r^2$ singlet could be hybridized. As discussed briefly later, the degeneracy in the $\{yz, xz\}$ doublet and in the $\{xy, x^2 - y^2\}$ doublet could be lifted by the crystal field. Such band splitting is also induced by the difference between t_{δ} and t_{π} . Further, all d orbitals could in principle be mixed by the SOC. Including these complexities is possible but depends on the material and they usually induce smaller perturbations, therefore, left for future analyses.

By diagonalizing the single-particle Hamiltonian $H_t + H_{soc}$, one obtains dispersion relations as shown in Fig. 2. In the simplest case, where the hopping matrix $t_{\mathbf{r}\mathbf{r}'}^{\alpha\beta}$ does not distinguish t_{δ} and t_{π} and the SOC is absent, the dispersion relation is identical to the one for the single-band tight-binding model, consisting of flat bands and graphene-like bands as shown by gray lines in Fig. 2 (a).

Note that each band is fourfold degenerate because of two orbitals and two spins per site. Including SOC does not change the dispersion curve but simply shifts $\vec{l} \cdot \vec{s} = \pm 1/2$ bands (see supplementary information [57]).

Including orbital dependence as $t_{\delta} \neq t_{\pi}$ without SOC instead splits fourfold degeneracy except for two points at the Γ point and two points at the K point. Quite intriguingly, Dirac dispersions emerge from the topmost flat bands as shown as blue lines in Fig. 2 (a). Turning on the SOC further splits such fourfold degeneracy, leading to nontrivial band topology. In this particular example, the spin component along the z axis is conserved giving unique characteristics to this case. As shown in Fig. 2 (b), the spin up component of each band is characterized by a nonzero Chern number \mathcal{C}_n . Because of the time-reversal symmetry, spin down bands have opposite Chern numbers. The topological property is also confirmed by gapless modes in the dispersion relation with the ribbon geometry as shown in Fig. 2 (c). Here, there appear one (two) pair of gapless modes between the highest and the second highest (between the second lowest and the third lowest) bands as shown as red (blue) curves, corresponding to the sum of Chern numbers below the gap, $-1(-2)$.

A multi-orbital kagomé model thus naturally shows quasi flat bands with nontrivial topology. However, close inspection revealed that, with $t_{\delta} = 0.5$ and $\lambda = 0.2$, the minimum of the highest band at the K point is slightly lower than the maximum of the second highest band at the Γ point. Thus, instead of a TI, a topological semimetal is realized when the Fermi level is located between the highest band and the second highest band. In fact, there are ways to make the gap positive. Here, we consider second-neighbor hopping matrices $\hat{t}_{\mathbf{r}\mathbf{r}'}^{(2)}$. As detailed in the supplementary information [57], these are also parametrized by π -bonding ($dd\pi$) and δ -bonding ($dd\delta$), $t_{\pi}^{(2)}$ and $t_{\delta}^{(2)}$, respectively. For simplicity, we fix the ratio between t_{π} and $t_{\pi}^{(2)}$ and between t_{δ} and $t_{\delta}^{(2)}$ as $t_{\pi}^{(2)}/t_{\pi} = t_{\delta}^{(2)}/t_{\delta} = r_2$, and analyze the sign and magnitude of the band gap Δ_{gap} between the highest band and the second highest band, as well as the flatness of the highest band defined by $\Delta\varepsilon \equiv \varepsilon_{1,max} - \varepsilon_{1,min}$.

Figure 3 (a) plots $\Delta\varepsilon$ as a function of t_{δ} and r_2 with $\lambda = 0.2$. As mentioned previously, the perfectly flat band with $\Delta\varepsilon = 0$ is realized at $t_{\delta} = 1$ and $r_2 = 0$, but band gap Δ_{gap} is zero. The flatness is immediately degraded by reducing t_{δ} from 1. As indicated by an open square in the plot, $t_{\delta} = 0.5$ and $r_2 = 0$ gives $\Delta\varepsilon \sim 0.88$ and negative band gap $\Delta_{gap} \sim -0.027$. Nonzero r_2 controls the relative energy between the zone center and the zone boundary. In particular, negative r_2 pushes up the energy at the K point, hereby the flatness is recovered. Naturally, the flatness and the positive gap are correlated as indicated by red loops in the second and forth quadrants because the separation between the highest band and the second highest band is fixed by the SOC strength. As indicated by a filled circle, $t_{\delta} = 0.5$ and $r_2 = -0.2$ gives $\Delta\varepsilon \sim 0.22$ and positive band gap $\Delta_{gap} \sim 0.17$. Corre-

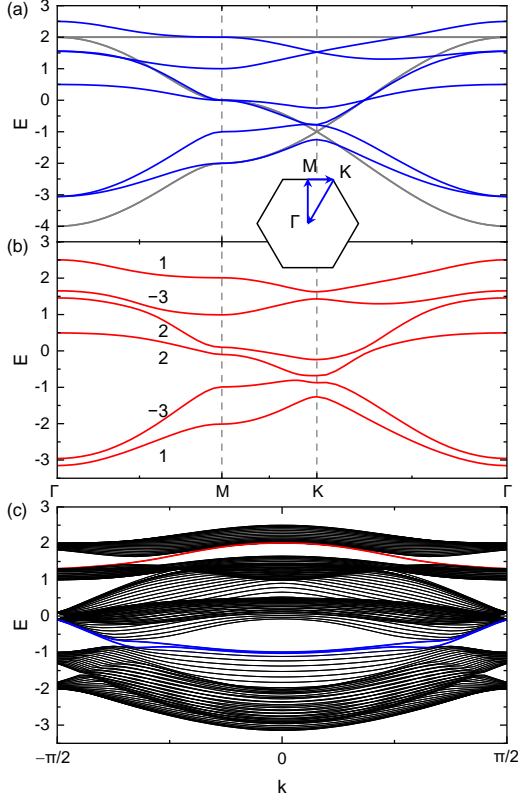


FIG. 2: Bulk dispersion relations without the SOC (a) and with the SOC with $\lambda = 0.2$ (b). In both case, energy is scaled by t_π . Gray lines in (a) indicate the dispersion with $t_\delta = 1$, which realizes ideal dispersion in a kagomé lattice. Blue and red lines are dispersions with $t_\delta = 0.5$, shown in (b). The inset shows high-symmetry lines in the first Brillouin zone. Chern number \mathcal{C}_n for the spin up component of each band is also shown in (b). (c) Dispersion relations with $t_\delta = 0.5$ and $\lambda = 0.2$ in the ribbon geometry, which is periodic along the \mathbf{a}_1 direction and contains 20 unit cells along the perpendicular direction.

sponding dispersion relation is shown in Fig. 3 (b). The Chern numbers remain unchanged by this r_2 .

Interacting model.—Having established the topological property on the single-particle level, we turn our attention to many-body effects focusing on the highest-energy flat band. A unique property of the current model is that the topmost quasi flat band has Chern number $|\mathcal{C}| = 1$. Thus, a large spin polarization can be induced by many-body interactions [58] or by a small magnetic field. Further intriguing possibilities are FQH states or fractional Chern insulating states when a topological flat band has a fractional filling and the insulating gap is induced by correlation effects [44, 46–52]. We examine such a possibility in our kagomé model. Assuming the spin polarization in the highest band, we introduce local and nearest-neighbor Coulomb repulsive interactions as $H_U = U \sum_{\mathbf{r}} n_{\mathbf{r}\uparrow} n_{\mathbf{r}\downarrow} + V \sum_{\langle \mathbf{r}\mathbf{r}' \rangle} \sum_{\alpha\beta} n_{\mathbf{r}\alpha\uparrow} n_{\mathbf{r}'\beta\uparrow}$, where $n_{\mathbf{r}\alpha\sigma} = c_{\mathbf{r}\alpha\sigma}^\dagger c_{\mathbf{r}\alpha\sigma}$. These interactions are then projected

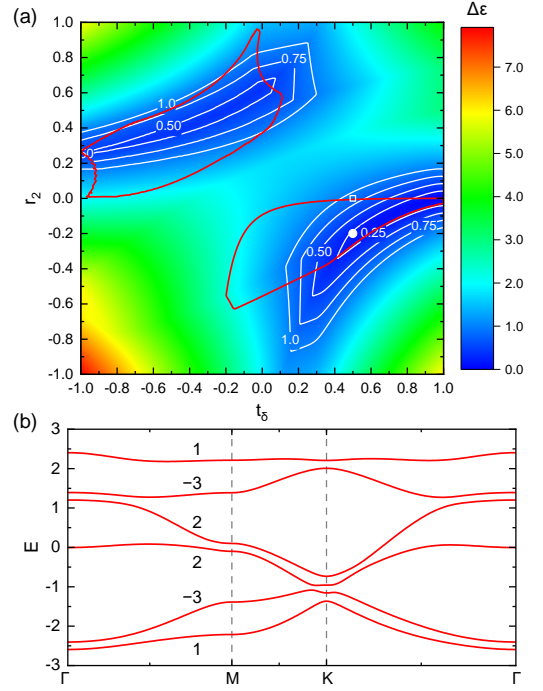


FIG. 3: (a) Flatness of the highest band $\Delta\epsilon$ as a function of t_δ and r_2 with $\lambda = 0.2$. Open square (filled circle) locates $t_\delta = 0.5$ with $r_2 = 0$ (-0.2). Red closed loops show the areas where the band gap is positive $\Delta_{gap} > 0$. (b) Bulk band structure with $t_\delta = 0.5$, $r_2 = -0.2$, and $\lambda = 0.2$. Band-dependent Chern number is also shown.

onto the highest band, leading to the effective Hamiltonian $H_{eff} = H_t + H_{soc} + H_U$.

Note that the S_z conservation is not essential to realize FQH. For our case and most of others, including complexities which break S_z conservation does not destroy FQH as long as the flat band has the nontrivial topology and is well separated from other bands, justifying projecting interaction terms onto the flat band and allowing for an accurate Lanczos calculation. While computational cost would be expensive, direct calculations of multiband models with S_z -non-conserving terms would show FQH if appropriate condition is fulfilled, but this possibility has not been fully explored, yet.

The effective Hamiltonian H_{eff} is diagonalized in momentum space. For this purpose, we discretize the momentum space into $N_1 \times N_2$ patches and express the Hamiltonian in the occupation basis, i.e., the Hilbert space is built up by $|\varphi_l\rangle = \prod_{\mathbf{k} \in l} \psi_{1\mathbf{k}}^\dagger |0\rangle$, where $\psi_{1\mathbf{k}}$ is the single-particle wave function for the highest flat band at momentum \mathbf{k} , and the combination of \mathbf{k} is specified by l . Due to the translational symmetry and the momentum conservation of many-body interaction terms, H_{eff} is subdiagonalized according to the total momentum $\mathbf{k}_{tot} = \langle \varphi_l | \sum_{\mathbf{k}} \mathbf{k} | \varphi_l \rangle$ modulo \mathbf{b}_1 and \mathbf{b}_2 , with $\mathbf{b}_{1,2}$ being two reciprocal lattice vectors. In this study, we take $N_1 = 4$ and $N_2 = 6$ and consider $\nu = 1/3$ filling,

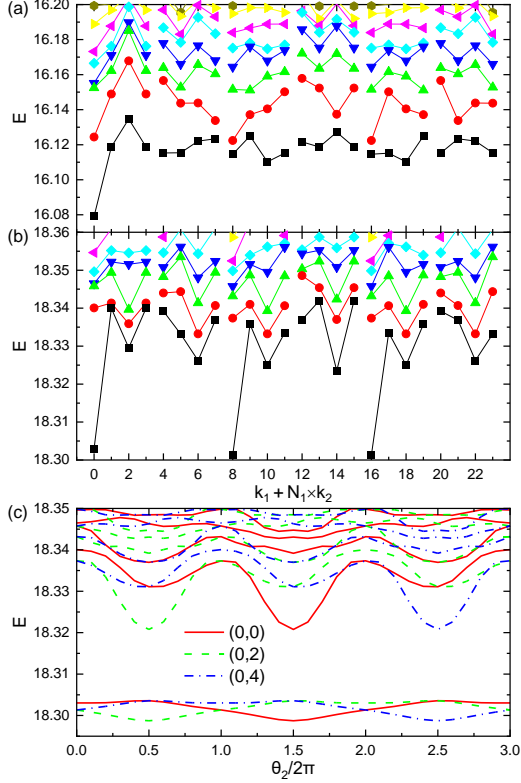


FIG. 4: Low-energy spectra of an interacting model with $t_\delta = 0.5$ with $r_2 = 0$ (a) and $r_2 = -0.2$ (b). Other parameter values are $\lambda = 0.2$, $U = 2$, and $V = 1$. (c) Spectral flow of the GSM upon flux insertion with $t_\delta = 0.5$ with $r_2 = -0.2$.

that is, the number electrons in the highest flat band is $N_e = 8$. Momentum sector will be specified using integer index (k_1, k_2) corresponding to the total momentum $\mathbf{k}_{tot} = \mathbf{b}_1 k_1 / N_1 + \mathbf{b}_2 k_2 / N_2$.

Figures 4 (a) and (b) show the low-energy spectra of the interacting model with $t_\delta = 0.5$ and $r_2 = 0$ and $t_\delta = 0.5$ and $r_2 = -0.2$, respectively, with $U = 2$ and $V = 1$ as a function of total momentum. In (a), the energy spectrum has a unique ground state at total momentum $(k_1, k_2) = (0, 0)$. (Note that this is to show the competition between the wide band width and the correlation effects on the highest band.) When r_2 is introduced as -0.2 , the highest band becomes flatter, leading to a drastic change in the energy spectrum. There appear three energy minima at $(k_1, k_2) = (0, 0)$, $(0, 2)$, and $(0, 4)$, forming a threefold degenerate ground state manifold (GSM), which is separated from the other states by an energy gap ~ 0.03 . As shown in Fig. 4 (c), the three sectors evolve with each other by inserting magnetic fluxes without having overlap with higher energy states (energy separation is slightly reduced to ~ 0.02). These results strongly suggest a $\nu = 1/3$ FQH state.

To confirm that this threefold degenerate ground state really represents a FQH state instead of trivial states such as charge density waves, we compute Chern num-

ber $\mathcal{C}_{(k_1, k_2)}$ by introducing a twist boundary condition [5]. Here, we discretize the boundary phase unit cell into 20×20 meshes, and numerically evaluate the Berry curvature as detailed in Ref. [57]. From this analysis, we obtain $\mathcal{C}_{(0,0)} = 0.331489$, $\mathcal{C}_{(0,2)} = 0.330318$, $\mathcal{C}_{(0,4)} = 0.338193$, and the sum of the three Chern numbers exactly 1 within the numerical accuracy. A slight deviation from the ideal value $\mathcal{C} = 1/3$ is ascribed to the finite size effect. This proves the $\nu = 1/3$ FQH phase with a quantized fractional Hall response $\sigma_H = \frac{1}{3}e^2/h$.

Discussion.—In this work, we considered an itinerant electron model on a kagomé lattice with twofold degenerate orbitals per site. However, each site has C_2 rotational symmetry, rather than C_3 or C_4 . Thus, the degeneracy between the two orbitals (yz and xz) can be lifted. In our tight-binding model, a difference in the hopping amplitude between t_π and t_δ in fact lifts such degeneracy, leading to the splitting in the band structure. Thus, adding local crystal field splitting, which respects the underlying lattice symmetry, would not fully destroy the topological property found in this work, while the position of topological or flat bands would be modified depending on the model parameters. As a number of kagomé materials have already indicated the nontrivial band topology [21–24, 26–28, 30–32, 36–39], reducing the thickness of such materials down to few unit cells or growing thin films of such materials and tuning the Fermi level to a topological flat band by the chemical substitution or gating might be a promising route to observe the predicted phenomena. The sign and the magnitude of parameter r_2 could depend on the detail of the material, such as species of ligand ions, and might be further controlled by compressive or tensile strain. First principles calculations would help to construct realistic material-dependent models [12, 15, 17]. In addition to a kagomé lattice, topological flat bands appear in dice and Lieb lattices [59–61]. Study of FQH or fractional Chern insulating states in such lattice geometries and material search is another important direction.

To summarize, we demonstrated the close interplay between the spatial frustration and the orbital degree of freedom in a kagomé lattice. With the relativistic spin-orbit coupling, such an interplay not only affects the band dispersion, but also induces nontrivial topology. Specifically, we showed that the original flat bands in a kagomé lattice become dispersive and topologically nontrivial. When such topological bands are fractionally occupied by electrons, many-body interactions drive further intriguing phenomena, i.e., fractional quantum Hall states or fractional Chern insulating states. Our work may bridge the gap between idealized theoretical studies and real materials.

Acknowledgments

The research of S.O., N.M., and E.D. was supported by the U.S. Department of Energy, Office of Science, Basic

Energy Sciences, Materials Sciences and Engineering Division. D.N.S was supported by the U.S. Department of Energy, Office of Basic Energy Sciences under Grant No. DE-FG02-06ER46305 for numerical studies of topological interacting systems. S.O. thanks H. Miao and H. Li

for discussions. This research used resources of the Compute and Data Environment for Science (CADES) at the Oak Ridge National Laboratory, which is supported by the Office of Science of the U.S. Department of Energy under Contract No. DE-AC05-00OR22725.

-
- [1] E. H. Lieb, Phys. Rev. Lett. **62**, 1201 (1989).
- [2] A. Mielke, J. Phys. A: Math. Gen. **24**, L73; **24**, 3311 (1991); **25**, 4335 (1992).
- [3] H. Tasaki, Phys. Rev. Lett. **69**, 1608 (1992).
- [4] A. Mielke and H. Tasaki, Commun. Math. Phys. **158**, 341 (1993).
- [5] D. J. Thouless, M. Kohmoto, M. P. Nightingale, and M. den Nijs, Phys. Rev. Lett. **49**, 405 (1982).
- [6] F. D. M. Haldane, Phys. Rev. Lett. **61**, 2015 (1988).
- [7] C. L. Kane and E. J. Mele, Phys. Rev. Lett. **95**, 146802 (2005).
- [8] B. A. Bernevig, T. L. Hughes, and S.-C. Zhang, Science **314**, 1757 (2006).
- [9] K. Ohgushi, S. Murakami, and N. Nagaosa, Phys. Rev. B **62**, R6065 (2000).
- [10] H. M. Guo and M. Franz, Phys. Rev. B **80**, 113102 (2009).
- [11] J. Wen, A. Rugg, C. C. Wang, and G. A. Fiete, Phys. Rev. B **82**, 075125 (2010).
- [12] Z. Liu, Z. F. Wang, J. W. Mei, Y. S. Wu, and F. Liu, Phys. Rev. Lett. **110**, 106804 (2013).
- [13] M. L. Kiesel, C. Platt, and R. Thomale, Phys. Rev. Lett. **110**, 126405 (2013).
- [14] I. I. Mazin, H. O. Jeschke, F. Lechermann, H. Lee, M. Fink, R. Thomale, and R. Valenti, Nat. Commun. **5**, 4261 (2014).
- [15] M. Zhou, Z. Liu, W. Ming, Z. Wang, and F. Liu, Phys. Rev. Lett. **113**, 236802 (2014).
- [16] G. Xu, B. Lian, and S.-C. Zhang, Phys. Rev. Lett. **115**, 186802 (2015).
- [17] M. G. Yamada, T. Soejima, N. Tsuji, D. Hirai, M. Dinca, and H. Aoki, Phys. Rev. B **94**, 081102(R) (2016).
- [18] A. Bolens, and N. Nagaosa, Phys. Rev. B **99**, 165141 (2019).
- [19] X. Wan, A. M. Turner, A. Vishwanath, and S. Y. Savrasov, Phys. Rev. B **83**, 205101 (2011).
- [20] S.-Y. Xu, I. Belopolski, N. Alidoust, M. Neupane, G. Bian, C. Zhang, R. Sankar, G. Chang, Z. Yuan, C.-C. Lee, S.-M. Huang, H. Zheng, J. Ma, D. S. Sanchez, B. Wang, A. Bansil, F. Chou, P. P. Shibayev, H. Lin, S. Jia, and M. Zahid Hasan, Science **349**, 613 (2015).
- [21] J. M. Allred, S. Jia, M. Bremholm, B. C. Chan, and R. J. Cava, Journal of Alloys and Compounds **539**, 137 (2012).
- [22] J.-X. Yin, S. S. Zhang, G. Chang, Q. Wang, S. S. Tsirkin, Z. Guguchia, B. Lian, H. Zhou, K. Jiang, I. Belopolski, N. Shumiya, D. Multer, M. Litskevich, T. A. Cochran, H. Lin, Z. Wang, T. Neupert, S. Jia, H. Lei, and M. Zahid Hasan, Nat. Phys. **15**, 443 (2019).
- [23] L. Jiao, Q. Xu, Y. Cheon, Y. Sun, C. Felser, E. Liu, and S. Wirth, Phys. Rev. B **99**, 245158 (2019).
- [24] D. F. Liu, A. J. Liang, E. K. Liu, Q. N. Xu, Y. W. Li, C. Chen, D. Pei, W. J. Shi, S. K. Mo, P. Dudin, T. Kim, C. Cacho, G. Li, Y. Sun, L. X. Yang, Z. K. Liu, S. S. P. Parkin, C. Felser, and Y. L. Chen, Science **365**, 1282 (2019).
- [25] W. R. Meier, M.-H. Du, S. Okamoto, N. Mohanta, A. F. May, M. A. McGuire, C. A. Bridges, G. D. Samolyuk, and B. C. Sales, Phys. Rev. B **102**, 075148 (2020).
- [26] Z. Lin, J.-H. Choi, Q. Zhang, W. Qin, S. Yi, P. Wang, L. Li, Y. Wang, H. Zhang, Z. Sun, L. Wei, S. Zhang, T. Guo, Q. Lu, J.-H. Cho, C. Zeng, and Z. Zhang, Phys. Rev. Lett. **121**, 096401 (2018).
- [27] L. Ye, M. Kang, J. Liu, F. von Cube, C. R. Wicker, T. Suzuki, C. Jozwiak, A. Bostwick, E. Rotenberg, D. C. Bell, L. Fu, R. Comin, and J. G. Checkelsky, Nature (London) **555**, 638 (2018).
- [28] M. Kang, L. Ye, S. Fang, J.-S. You, A. Levitan, M. Han, J. I. Facio, C. Jozwiak, A. Bostwick, E. Rotenberg, M. K. Chan, R. D. McDonald, D. Graf, K. Kaznatcheev, E. Vescovo, D. C. Bell, E. Kaxiras, J. van den Brink, M. Richter, M. P. Ghimire, J. G. Checkelsky, and R. Comin, Nat. Mater. **19**, 163 (2020).
- [29] B. C. Sales, J. Yan, W. R. Meier, A. D. Christianson, S. Okamoto, and M. A. McGuire, Phys. Rev. Materials **3**, 114203 (2019).
- [30] S. Nakatsuji, N. Kiyohara, and T. Higo, Nature (London) **527**, 212 (2015).
- [31] A. K. Nayak, J. E. Fischer, Y. Sun, B. Yan, J. Karel, A. C. Komarek, C. Shekhar, N. Kumar, W. Schnelle, J. Kubler, C. Felser, and S. S. P. Parkin, Sci. Adv. **2**, e1501870 (2016).
- [32] K. Kuroda, T. Tomita, M.-T. Suzuki, C. Bareille, A. A. Nugroho, P. Goswami, M. Ochi, M. Ikhlas, M. Nakayama, S. Akebi, R. Noguchi, R. Ishii, N. Inami, K. Ono, H. Kumigashira, A. Varykhalov, T. Muro, T. Koretsune, R. Arita, S. Shin, T. Kondo, and S. Nakatsuji, Nat. Mater. **16**, 1090 (2017).
- [33] S. Park, S. Kang, H. Kim, K. H. Lee, P. Kim, S. Sim, N. Lee, B. Karuppannan, J. Kim, J. Kim, K. I. Sim, M. J. Coak, Y. Noda, C.-H. Park, J. H. Kim, and J.-G. Park, Sci. Rep. **10**, 20998 (2020).
- [34] S. Taie, H. Ozawa, T. Ichinose, T. Nishio, S. Nakajima, and Y. Takahashi, Sci. Adv. **1**, e1500854 (2015).
- [35] R. Drost, T. Ojanen, A. Harju, and P. Liljeroth, Nat. Phys. **13**, 668 (2017).
- [36] B. R. Ortiz, S. M. L. Teicher, Y. Hu, J. L. Zuo, P. M. Sarte, E. C. Schueller, A. M. Milinda Abeykoon, M. J. Krogstad, S. Rosenkranz, R. Osborn, R. Seshadri, L. Balents, J. He, and S. D. Wilson, Phys. Rev. Lett. **125**, 247002 (2020).
- [37] X. Wu, T. Schwemmer, T. Muller, A. Consiglio, G. Sangiovanni, D. Di Sante, Y. Iqbal, W. Hanke, A. P. Schnyder, M. M. Denner, M. H. Fischer, T. Neupert, and R. Thomale, Phys. Rev. Lett. **127**, 177001 (2021).
- [38] X. Feng, K. Jiang, Z. Wang, and J. Hu, Sci. Bull. **66**, 1384 (2021).
- [39] M. M. Denner, R. Thomale, and T. Neupert, Phys. Rev. Lett. **127**, 217601 (2021).

- [40] D. C. Tsui, H. L. Stormer, and A. C. Gossard, Phys. Rev. Lett. **48**, 1559 (1982).
- [41] R. B. Laughlin, Phys. Rev. Lett. **50**, 1395 (1983).
- [42] D. Yoshioka, B. I. Halperin, and P. A. Lee, Phys. Rev. Lett. **50**, 1219 (1983).
- [43] J. K. Jain, Phys. Rev. Lett. **63**, 199 (1989).
- [44] E. Tang, J.-W. Mei, and X.-G. Wen, Phys. Rev. Lett. **106**, 236802 (2011).
- [45] Y.-L. Wu, B. A. Bernevig, and N. Regnault, Phys. Rev. B **85**, 075116 (2012).
- [46] K. Sun, Z. Gu, H. Katsura, and S. Das Sarma, Phys. Rev. Lett. **106**, 236803 (2011).
- [47] T. Neupert, L. Santos, C. Chamon, and C. Mudry, Phys. Rev. Lett. **106**, 236804 (2011).
- [48] D. N. Sheng, Z.-C. Gu, K. Sun, and L. Sheng, Nat. Commun. **2**, 389 (2011).
- [49] Y.-F. Wang, Z.-C. Gu, C.-D. Gong, and D. N. Sheng, Phys. Rev. Lett. **107**, 146803 (2011).
- [50] N. Regnault and B. A. Bernevig, Phys. Rev. X **1**, 021014 (2011).
- [51] D. Xiao, W. Zhu, Y. Ran, N. Nagaosa, and S. Okamoto, Nat. Commun. **2**, 596 (2011).
- [52] J. W. F. Venderbos, S. Kourtis, J. van den Brink, and M. Daghofer, Phys. Rev. Lett. **108**, 126405 (2012).
- [53] Y.-H. Wu, J. K. Jain, and K. Sun, Phys. Rev. B **86**, 165129 (2012).
- [54] G. Moore and N. Read, Nucl. Phys. B **360** 362 (1991).
- [55] C. Nayak, S. H. Simon, A. Stern, M. Freedman, and S. Das Sarma, Rev. Mod. Phys. **80**, 1083 (2008).
- [56] J. C. Slater and G. F. Koster, Phys. Rev. **94**, 1498 (1954).
- [57] For the detail of our theoretical model and numerical calculations, see the supplementary information.
- [58] E. C. Stoner, Proc. R. Soc. London A **165**, 372 (1938).
- [59] F. Wang and Y. Ran, Phys. Rev. B **84**, 241103(R) (2011).
- [60] R. Soni, N. Kaushal, S. Okamoto, and E. Dagotto, Phys. Rev. B **102**, 045105 (2020).
- [61] R. Soni, A. B. Sanyal, N. Kaushal, S. Okamoto, A. Moreo, and E. Dagotto, Phys. Rev. B **104**, 235115 (2021).

Supplementary material: Topological flat bands in a kagomé lattice multiorbital system

Satoshi Okamoto,¹ Narayan Mohanta,¹ Elbio Dagotto,^{1,2} and D. N. Sheng³

¹*Materials Science and Technology Division, Oak Ridge National Laboratory, Oak Ridge, Tennessee 37831, USA*

²*Department of Physics and Astronomy, The University of Tennessee, Knoxville, Tennessee 37996, USA*

³*Department of Physics and Astronomy, California State University, Northridge, California 91330, USA*

S1. NON-INTERACTING CASE

1. $\{yz, xz\}$ model

Here we deduce the hopping matrices of the $\{yz, xz\}$ model in the Slater-Koster approximation. For nearest-neighbor bonds, in addition to the diagonal matrix $\hat{t}_{\mathbf{1}\mathbf{2}}$ presented in the main text, we have

$$\begin{aligned}\hat{t}_{\mathbf{1}\mathbf{3}} &= \frac{1}{4} \begin{bmatrix} 3t_\pi + t_\delta & \sqrt{3}(t_\pi - t_\delta) \\ \sqrt{3}(t_\pi - t_\delta) & t_\pi + 3t_\delta \end{bmatrix}, \\ \hat{t}_{\mathbf{2}\mathbf{3}} &= \frac{1}{4} \begin{bmatrix} 3t_\pi + t_\delta & -\sqrt{3}(t_\pi - t_\delta) \\ -\sqrt{3}(t_\pi - t_\delta) & t_\pi + 3t_\delta \end{bmatrix}.\end{aligned}\quad (\text{S1})$$

Similarly, second neighbor hopping matrices can be written as

$$\begin{aligned}\hat{t}_{\mathbf{1}\mathbf{2}}^{(2)} &= \begin{bmatrix} t_\pi^{(2)} & 0 \\ 0 & t_\delta^{(2)} \end{bmatrix}, \\ \hat{t}_{\mathbf{1}\mathbf{3}}^{(2)} &= \frac{1}{4} \begin{bmatrix} t_\pi^{(2)} + 3t_\delta^{(2)} & -\sqrt{3}(t_\pi^{(2)} - t_\delta^{(2)}) \\ -\sqrt{3}(t_\pi^{(2)} - t_\delta^{(2)}) & 3t_\pi^{(2)} + t_\delta^{(2)} \end{bmatrix}, \\ \hat{t}_{\mathbf{2}\mathbf{3}}^{(2)} &= \frac{1}{4} \begin{bmatrix} t_\pi^{(2)} + 3t_\delta^{(2)} & \sqrt{3}(t_\pi^{(2)} - t_\delta^{(2)}) \\ \sqrt{3}(t_\pi^{(2)} - t_\delta^{(2)}) & 3t_\pi^{(2)} + t_\delta^{(2)} \end{bmatrix},\end{aligned}\quad (\text{S2})$$

where, subscript (2) is introduced to highlight the difference from the nearest-neighbor bonds. These are schematically shown in Fig. S1. $t_\pi^{(2)}$ and $t_\delta^{(2)}$ correspond to $(dd\pi)$ and $(dd\delta)$, respectively, in Ref. [S1].

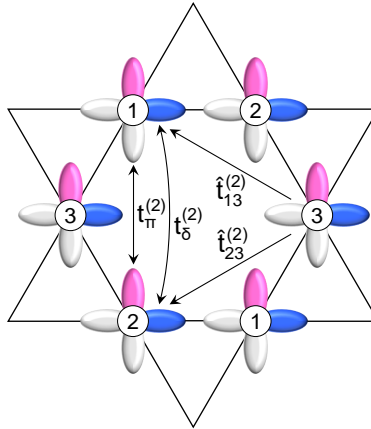


FIG. S1: Second neighbor hopping matrices.

Bulk dispersion relation for the simplest case with $t_\delta = 1$, $r_2 = 0$, and $\lambda = 0.2$ is presented in Fig. S2. With this set of parameters, the dispersion relation consists of two dispersions of ideal kagomé system with nearest-neighbor hopping separated by λ as each set of dispersions comes from $\vec{l} \cdot \vec{s} = 1/2$ or $\vec{l} \cdot \vec{s} = -1/2$ states.

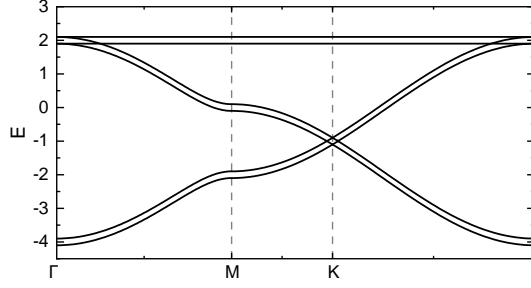


FIG. S2: Bulk dispersion with $t_\delta = 1$, $r_2 = 0$, and $\lambda = 0.2$.

Band-dependent Berry curvature of non-interacting electrons is given as a function of momentum \mathbf{k} as

$$\Omega_{n\mathbf{k}} = \frac{i}{2\pi} \sum_{m(\neq n)} \frac{\langle n|\hat{v}_{x\mathbf{k}}|m\rangle\langle m|\hat{v}_{y\mathbf{k}}|n\rangle - \langle n|\hat{v}_{y\mathbf{k}}|m\rangle\langle m|\hat{v}_{x\mathbf{k}}|n\rangle}{(\varepsilon_{m\mathbf{k}} - \varepsilon_{n\mathbf{k}})^2}, \quad (\text{S3})$$

where, using the Hamiltonian matrix in momentum space $\hat{H}_{\mathbf{k}}$, $\hat{v}_{\eta\mathbf{k}}$ is given by $\hat{v}_{\eta\mathbf{k}} = \partial\hat{H}_{\mathbf{k}}/\partial k_\eta$. With this Berry curvature, the band dependent Chern number \mathcal{C}_n is given by

$$\mathcal{C}_n = \frac{1}{(2\pi)^2} \int_{BZ} d^2k \Omega_{n\mathbf{k}}, \quad (\text{S4})$$

where the momentum integral is taken in the first Brillouin zone.

Figure S3 shows the band-dependent Berry curvature for $t_\delta = 0.5$ and $r_2 = 0$ with $\lambda = 0.2$, a parameter set used in Figs. 2 (b) and (c) in the main text. The momentum integral of each plot gives band-dependent Chern number as shown in Fig. 2 (b).

To examine the role of second-neighbor hoppings, we compute the flatness of the highest band defined by $\Delta\varepsilon \equiv \varepsilon_{1,max} - \varepsilon_{1,min}$ and the band gap defined by $\Delta_{gap} \equiv \varepsilon_{1,min} - \varepsilon_{2,max}$. Results are summarized in Figure S4. [Fig. 3 (a) in the main text is the combination of Figs. S4 (a) and (b).] In both plots, the location of $t_\delta = 0.5$ with $r_2 = 0$, the parameter set used in Fig. 2 (b) in the main text, is indicated by an open square, and the location of $t_\delta = 0.5$ with $r_2 = -0.2$, the parameter set used in Fig. 3 (b) in the main text, is indicated by a filled circle.

The Berry curvature of non-interacting electrons with $t_\delta = 0.5$ and $r_2 = -0.2$ with $\lambda = 0.2$ is presented in Fig. S5.

2. $\{xy, x^2 - y^2\}$ model

Here, we show that a two-orbital model involving xy and $x^2 - y^2$ orbitals, the $\{xy, x^2 - y^2\}$ model, has the same form as the $\{yz, xz\}$ model. In addition to t_π and t_δ , we introduce t_σ , corresponding to $(dd\sigma)$ in Ref. [S1]. Using these three parameters, the hopping matrices are given by

$$\begin{aligned} \hat{t}_{12} &= \frac{1}{4} \begin{bmatrix} 4t_\pi & 0 \\ 0 & 3t_\sigma + t_\delta \end{bmatrix}, \\ \hat{t}_{13} &= \frac{1}{16} \begin{bmatrix} 9t_\sigma + 4t_\pi + 3t_\delta & -\sqrt{3}(3t_\sigma - 4t_\pi + t_\delta) \\ -\sqrt{3}(3t_\sigma - 4t_\pi + t_\delta) & 3t_\sigma + 12t_\pi + t_\delta \end{bmatrix}, \\ \hat{t}_{23} &= \frac{1}{4} \begin{bmatrix} 9t_\sigma + 4t_\pi + 3t_\delta & \sqrt{3}(3t_\sigma - 4t_\pi + t_\delta) \\ \sqrt{3}(3t_\sigma - 4t_\pi + t_\delta) & 3t_\sigma + 12t_\pi + t_\delta \end{bmatrix}. \end{aligned} \quad (\text{S5})$$

Defining $\tilde{t}_\sigma = \frac{1}{4}(3t_\sigma + t_\delta)$, these matrices are simplified as

$$\begin{aligned} \hat{t}_{12} &= \begin{bmatrix} t_\pi & \\ & \tilde{t}_\sigma \end{bmatrix}, \\ \hat{t}_{13} &= \frac{1}{4} \begin{bmatrix} 3\tilde{t}_\sigma + t_\pi & -\sqrt{3}(\tilde{t}_\sigma - t_\pi) \\ -\sqrt{3}(\tilde{t}_\sigma - t_\pi) & \tilde{t}_\sigma + 3t_\pi \end{bmatrix}, \\ \hat{t}_{23} &= \frac{1}{4} \begin{bmatrix} 3\tilde{t}_\sigma + t_\pi & \sqrt{3}(\tilde{t}_\sigma - t_\pi) \\ \sqrt{3}(\tilde{t}_\sigma - t_\pi) & \tilde{t}_\sigma + 3t_\pi \end{bmatrix}. \end{aligned} \quad (\text{S6})$$

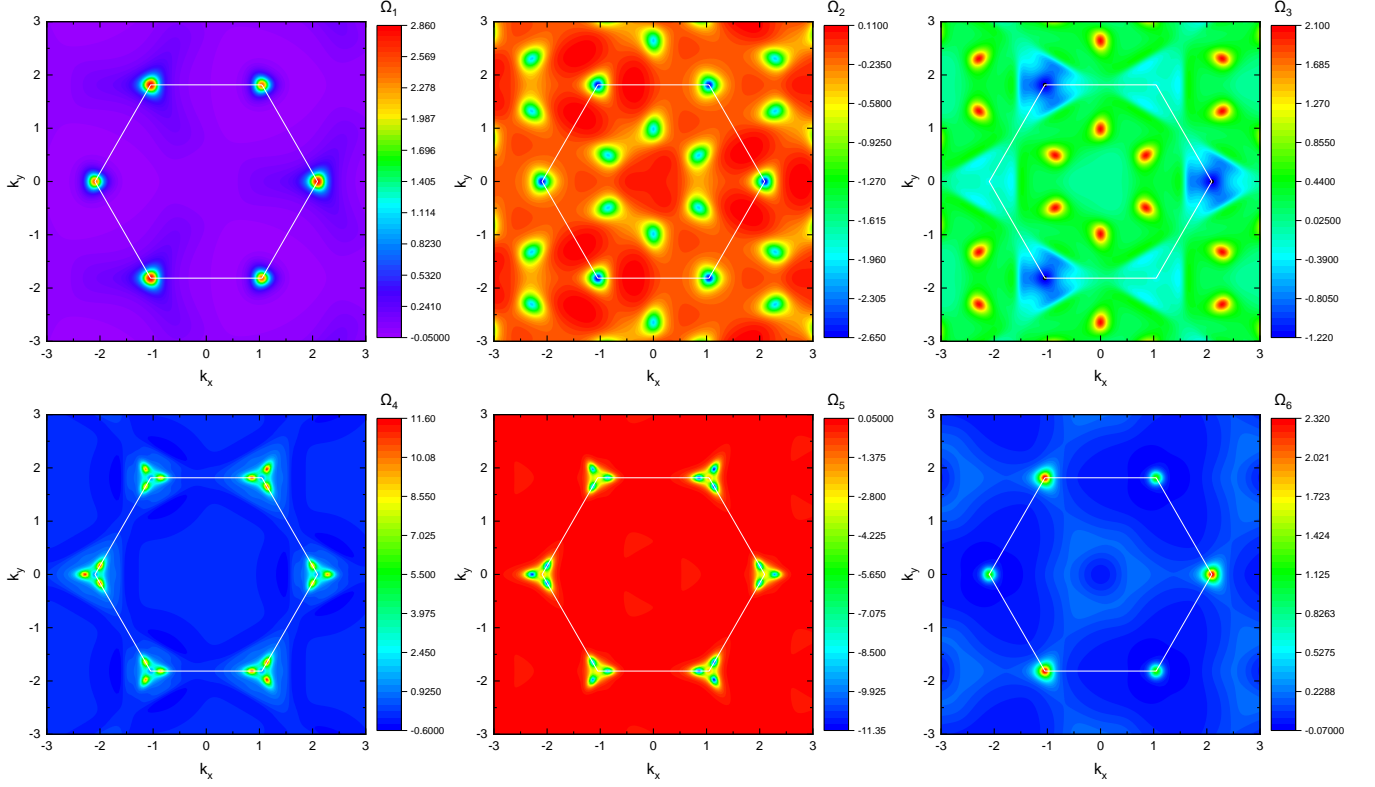


FIG. S3: Berry curvature of up bands with $t_\delta = 0.5$ and $\lambda = 0.2$ from the highest band Ω_1 to the lowest band Ω_6 . White lines indicate the first Brillouin zone. Berry curvature of down bands have negative value with the sign of momentum changed, $\Omega_i(k_x, k_y) \rightarrow -\Omega_i(-k_x, -k_y)$.

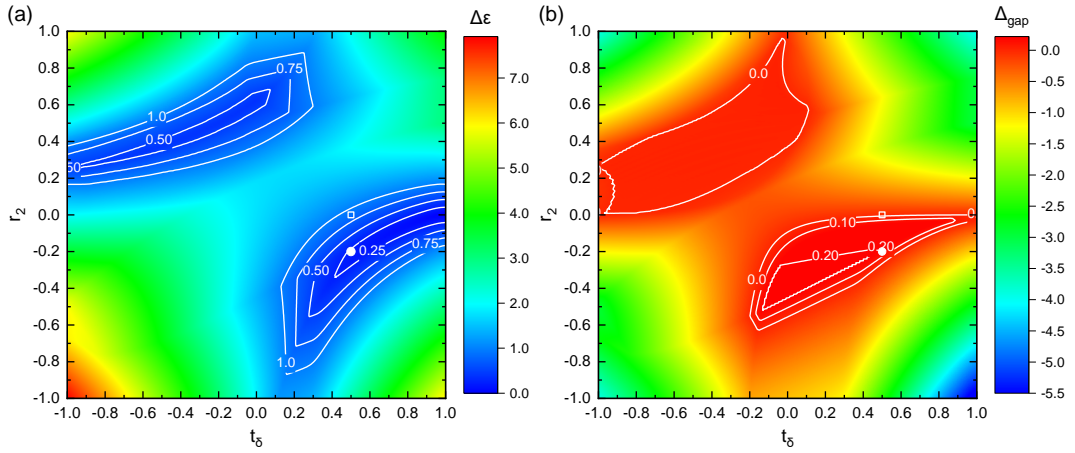


FIG. S4: (a) Flatness of the highest band and (b) gap amplitude between the highest band and the second highest band as functions of t_δ and r_2 with $\lambda = 0.2$.

A hopping matrix between site 1 and site 2 is schematically shown in Fig. S6. One notices that these matrices are identical to the hopping matrices for $\{yz, xz\}$ via $(\tilde{t}_\sigma, t_\pi) \rightarrow (t_\pi, t_\delta)$ with the change in sign in the off-diagonal elements.

Using the eigenstate of angular momentum $l_z = \pm 2$ for $l = 2$, the orbitals $|xy\rangle$ and $|x^2 - y^2\rangle$ are expressed as $|xy\rangle = -\frac{i}{\sqrt{2}}(|2\rangle + |-2\rangle)$ and $|x^2 - y^2\rangle = \frac{1}{\sqrt{2}}(|2\rangle - |-2\rangle)$, respectively. Using these relations, the SOC term, $\lambda \vec{l} \cdot \vec{s}$, in

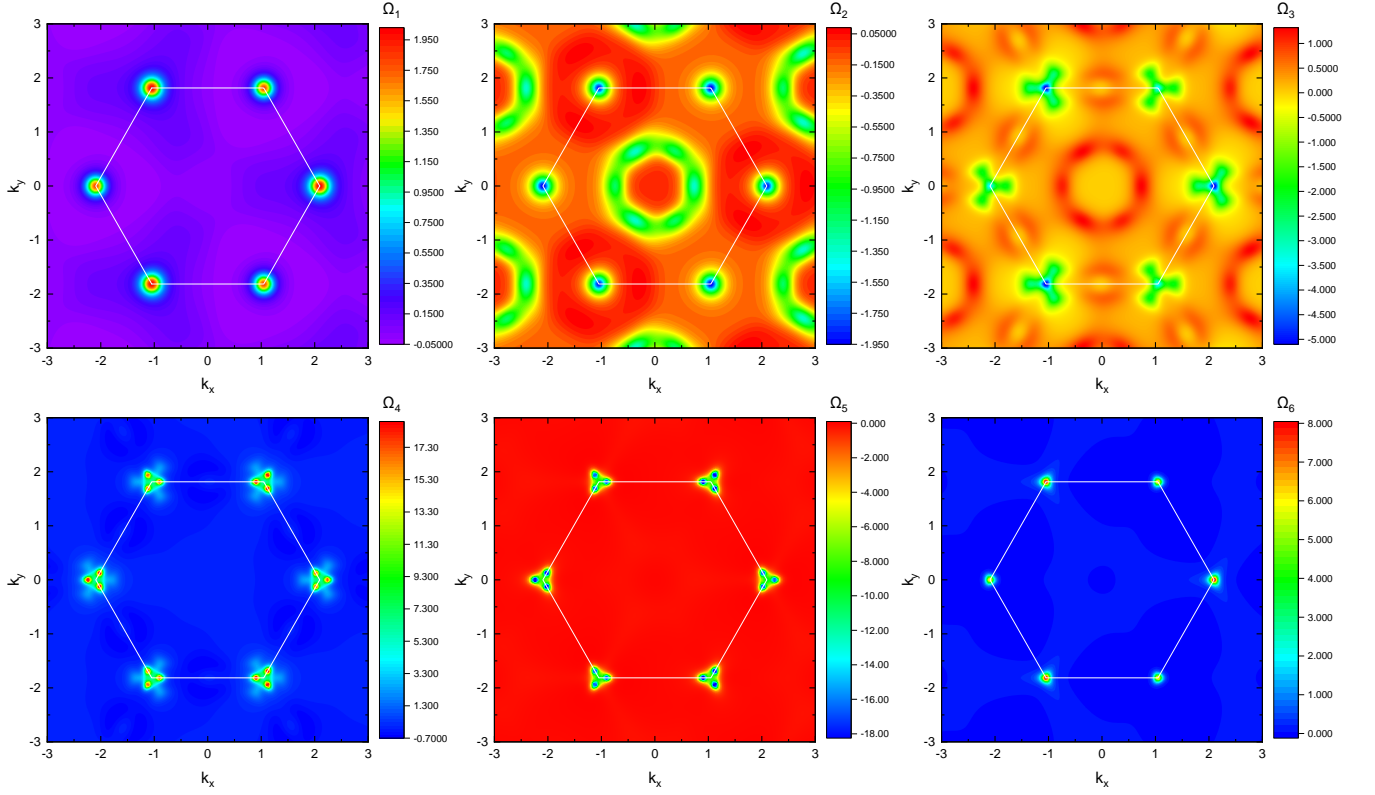


FIG. S5: Same as Fig. S3 but with $t_\delta = 0.5$ and $r_2 = -0.2$.

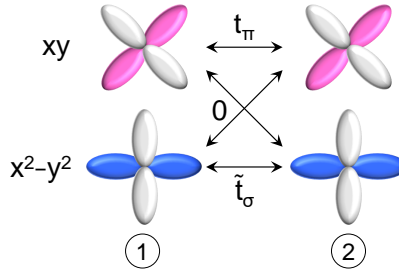


FIG. S6: Orbital dependent hopping matrix between site 1 and site 2 on a kagomé lattice.

the $\{xy, x^2 - y^2\}$ subset is written as

$$H_{soc} = \lambda \sum_{\mathbf{r}\sigma} \left(i\sigma_{\sigma\sigma}^z c_{\mathbf{r}a\sigma}^\dagger c_{\mathbf{r}b\sigma} + \text{H.c.} \right). \quad (\text{S7})$$

This form is also identical to the SOC in the $\{yz, xz\}$ model with a change in prefactor from $\frac{1}{2}\lambda$ to λ .

S2. MANY-BODY EFFECTS

This section discusses many-body effects in our kagomé model.

1. Effective Hamiltonian

In multi-orbital systems, the local Coulomb interactions consist of several terms. This is simplified in a spin polarized state, where interaction terms contain the single spin component as $H_U = U \sum_{\mathbf{r}} n_{\mathbf{r}\alpha\uparrow} n_{\mathbf{r}\beta\uparrow} + V \sum_{\langle \mathbf{r}\mathbf{r}' \rangle} \sum_{\alpha\beta} n_{\mathbf{r}\alpha\uparrow} n_{\mathbf{r}'\beta\uparrow}$.

Now we focus on the highest-energy up-spin band, which has the Chern number $\mathcal{C}_1 = 1$. The kinetic term is given by $\sum_{\mathbf{k}} \varepsilon_{1\mathbf{k}} \psi_{1\mathbf{k}}^\dagger \psi_{1\mathbf{k}}$, where $\psi_{1\mathbf{k}}^{(\dagger)}$ is an annihilation (creation) operator of an electron on the highest-energy band at momentum \mathbf{k} and energy $\varepsilon_{1\mathbf{k}}$. $\psi_{1\mathbf{k}}^{(\dagger)}$ and original electron operators $c_{\mathbf{k}\alpha\uparrow}^{(\dagger)} = \frac{1}{\sqrt{N_{uc}}} \sum_{\mathbf{r}} e^{-i\mathbf{k}\cdot\mathbf{r}} c_{\mathbf{r}\alpha\uparrow}^{(\dagger)}$ are related by the unitary transformation as $c_{\mathbf{k}\alpha\uparrow}^{(\dagger)} = U_{\alpha n}^{(*)}(\mathbf{k}) \psi_{n\mathbf{k}}^{(\dagger)}$, where, N_{uc} is the total number of unit cells, n is the band index. We apply this unitary transformation to H_U to obtain effective interactions in the highest band, i.e., $n = 1$. Since the full expression is rather lengthy, we provide only one example, local Coulomb interaction $U n_{\mathbf{r}\alpha\uparrow} n_{\mathbf{r}\beta\uparrow}$. This term becomes

$$\frac{1}{N_{uc}} U \sum_{\mathbf{k}_1, \mathbf{k}_2, \mathbf{k}_3, \mathbf{k}_4} U_{a1}^*(\mathbf{k}_1) U_{b1}^*(\mathbf{k}_2) U_{b1}(\mathbf{k}_3) U_{a1}(\mathbf{k}_4) \psi_{1\mathbf{k}_1}^\dagger \psi_{1\mathbf{k}_2}^\dagger \psi_{1\mathbf{k}_3} \psi_{1\mathbf{k}_4} \delta_{\mathbf{k}_1 + \mathbf{k}_2 - \mathbf{k}_3 - \mathbf{k}_4}, \quad (\text{S8})$$

where $\mathbf{k}_1 + \mathbf{k}_2 - \mathbf{k}_3 - \mathbf{k}_4$ in the δ function implies $\mathbf{k}_1 + \mathbf{k}_2 - \mathbf{k}_3 - \mathbf{k}_4$ modulo \mathbf{b}_1 and \mathbf{b}_2 , with $\mathbf{b}_{1,2}$ being two reciprocal lattice vectors. Using lattice translation vectors $\mathbf{a}_1 = (2, 0)$ and $\mathbf{a}_2 = (1, \sqrt{3})$, where the distance between nearest-neighbor sites is taken as the unit of length (see Fig. 1 in the main text), the reciprocal lattice vectors are given by $\mathbf{b}_1 = (\pi/\sqrt{3}, \pi)$ and $\mathbf{b}_2 = (0, 2\pi/\sqrt{3})$ (See Fig. S7). The effective Hamiltonian is thus constructed as

$$H_{eff} = \sum_{\mathbf{k}} \varepsilon_{1\mathbf{k}} \psi_{1\mathbf{k}}^\dagger \psi_{1\mathbf{k}} + \frac{1}{N_{uc}} \sum_{\mathbf{k}_1, \mathbf{k}_2, \mathbf{k}_3, \mathbf{k}_4} u(\mathbf{k}_1, \mathbf{k}_2, \mathbf{k}_3, \mathbf{k}_4) \psi_{1\mathbf{k}_1}^\dagger \psi_{1\mathbf{k}_2}^\dagger \psi_{1\mathbf{k}_3} \psi_{1\mathbf{k}_4} \delta_{\mathbf{k}_1 + \mathbf{k}_2 - \mathbf{k}_3 - \mathbf{k}_4}. \quad (\text{S9})$$

Here, $u(\mathbf{k}_1, \mathbf{k}_2, \mathbf{k}_3, \mathbf{k}_4)$ involves U and V with appropriate phase factors.

The effective Hamiltonian is diagonalized in momentum space. In this work, we consider a rhombus spanned by the two reciprocal lattice vectors and divide it into $N_1 \times N_2$ patches. This corresponds to having $N_{1(2)}$ unit cells along the $\mathbf{a}_{1(2)}$ direction, so $N_{uc} = N_1 \times N_2$. Discretized momenta are now expressed as $\mathbf{k} = \mathbf{b}_1 k_1 / N_1 + \mathbf{b}_2 k_2 / N_2$. We simply label discretized momenta using (k_1, k_2) . Figure S7 depicts the momentum discretization used in this study with $N_1 = 4, N_2 = 6$ and $N_{uc} = 24$.

In this study, we consider a fractional filling $\nu = 1/3$. With $N_{uc} = 24$, the number of electrons on the highest band is $N_e = N_{uc}/3 = 8$. In this case, the size of the Hilbert space is ${}_{24}C_8 = 735,471$. Due to the translational symmetry and the momentum conservation of many-body interaction terms, H_{eff} is subdiagonalized according to the total momentum, $\mathbf{k}_{tot} = \langle \varphi_l | \sum_{\mathbf{k}} \mathbf{k} | \varphi_l \rangle$ modulo \mathbf{b}_1 and \mathbf{b}_2 . Using the same notation as the momentum discretization (k_1, k_2) , each momentum sector has roughly $735,471/24 \approx 30,700$ states. $30,700 \times 30,700$ Hamiltonian matrices can be diagonalized efficiently using, for example, ARPACK [S3].

2. Many-body Chern number

The many-body Chern number is computed by introducing a twist boundary condition, $\psi(\mathbf{r} + N_j \mathbf{a}_j) = e^{i\theta_j} \psi(\mathbf{r})$ with phase factors $\theta_{j=1,2}$. This corresponds to inserting magnetic fluxes. When one flux quantum is inserted, θ_j changes from 0 to 2π and discretized momentum \mathbf{k} moves from its original position to its neighbor along the \mathbf{b}_j direction with the momentum shift given by $\Delta \mathbf{k} = \mathbf{b}_j / N_j$.

Many-body Chern number of the ground state (k_1, k_2) is computed via $\mathcal{C}_{(k_1, k_2)} = \frac{1}{2\pi} \int_0^{2\pi} d\theta_1 \int_0^{2\pi} d\theta_2 F_{(k_1, k_2)}(\theta_1, \theta_2)$ [S2] where $F(\theta_1, \theta_2)$ is the Berry curvature given by

$$F_{(k_1, k_2)}(\theta_1, \theta_2) = \text{Im} \left\{ \left\langle \frac{\partial \Phi_{(k_1, k_2)}}{\partial \theta_2} \right| \frac{\partial \Phi_{(k_1, k_2)}}{\partial \theta_1} \right\rangle - \left\langle \frac{\partial \Phi_{(k_1, k_2)}}{\partial \theta_1} \right| \frac{\partial \Phi_{(k_1, k_2)}}{\partial \theta_2} \right\rangle \right\}, \quad (\text{S10})$$

and $|\Phi_{(k_1, k_2)}\rangle$ is the many-body wave function. The momentum index (k_1, k_2) will be omitted in the following discussion for simplicity.

Partial derivative of a wave function with respect to θ_j is approximated by the finite difference as $|\partial \Phi / \partial \theta\rangle \approx \frac{1}{|\Delta \theta|} [|\Phi(\boldsymbol{\theta} + \Delta \boldsymbol{\theta})\rangle - |\Phi(\boldsymbol{\theta})\rangle]$. Here, the vector notation is used for $\boldsymbol{\theta} = (\theta_1, \theta_2)$, and $\Delta \boldsymbol{\theta} = (\Delta \theta_1, 0)$ or $(0, \Delta \theta_2)$. Then, it is required to compute a product of two wave functions as $\langle \Phi(\boldsymbol{\theta}) | \Phi(\boldsymbol{\theta}') \rangle$ with $\boldsymbol{\theta} \neq \boldsymbol{\theta}'$.

Since we are using a multiorbital model projected onto the flat band, a special care is needed. By diagonalizing a many-body Hamiltonian, the ground state in the momentum sector (k_1, k_2) is given by

$$|\Phi(\boldsymbol{\theta})\rangle = \sum_l V_{1l}(\boldsymbol{\theta}) |\varphi_l(\boldsymbol{\theta})\rangle, \quad (\text{S11})$$

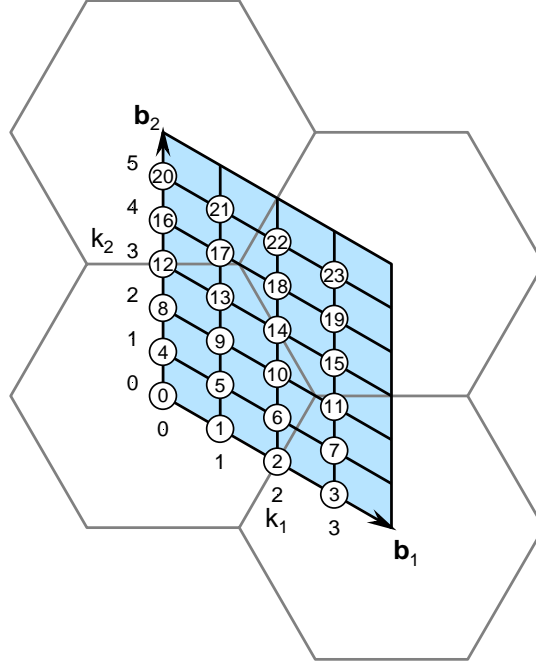


FIG. S7: Momentum discretization used in exact diagonalization calculations for an interacting model with $N_1 = 4$ and $N_2 = 6$. A number in a circle on each momentum is $k_1 + N_1 \times k_2$.

where, $V_{1l}(\theta)$ is the $(1, l)$ component of the unitary matrix, which diagonalizes the many-body Hamiltonian in the momentum sector (k_1, k_2) , and 1 means the ground state. $|\varphi_l(\theta)\rangle$ form the basis set to describe the many-body Hilbert space. Specifically, this is given by

$$|\varphi_l(\theta)\rangle = \prod_{\mathbf{k} \in l} \psi_{1\mathbf{k}+\Delta\mathbf{k}}^\dagger |0\rangle. \quad (\text{S12})$$

Here, $\psi_{1\mathbf{k}+\Delta\mathbf{k}}^\dagger$ is a creation operator of an electron at the highest flat band at momentum $\mathbf{k} + \Delta\mathbf{k}$, and $|0\rangle$ is the vacuum. Note that V matrices depend on the total momentum (k_1, k_2) , but U matrices do not because it is from diagonalising a single particle Hamiltonian. The product over \mathbf{k} is limited to a set of momenta specified by the index l . The momentum shift $\Delta\mathbf{k}$ and the twist phase θ are related via $\Delta\mathbf{k} = \mathbf{b}_1\theta_1/2\pi N_1 + \mathbf{b}_2\theta_2/2\pi N_2$. Recalling that a creation operator $\psi_{1\mathbf{k}}^\dagger$ is rewritten by creation operators of original electrons $c_{\mathbf{k}\alpha\uparrow}^\dagger$ as $\psi_{1\mathbf{k}}^\dagger = \sum_{\alpha} U_{\alpha 1}(\mathbf{k}) c_{\mathbf{k}\alpha\uparrow}^\dagger$, one finds

$$|\varphi_l(\theta)\rangle = \prod_{\mathbf{k} \in l} \left[\sum_{\alpha} U_{\alpha 1}(\mathbf{k} + \Delta\mathbf{k}) c_{\mathbf{k}+\Delta\mathbf{k}\alpha\uparrow}^\dagger \right] |0\rangle. \quad (\text{S13})$$

Using this, $\langle \Phi(\theta) | \Phi(\theta') \rangle$ is rewritten as

$$\begin{aligned} \langle \Phi(\theta) | \Phi(\theta') \rangle &= \langle 0 | \sum_l V_{1l}^*(\theta) \prod_{\mathbf{k} \in l} \left[\sum_{\alpha} U_{\alpha 1}^*(\mathbf{k} + \Delta\mathbf{k}) c_{\mathbf{k}+\Delta\mathbf{k}\alpha\uparrow} \right] \\ &\quad \times \sum_{l'} V_{1l'}(\theta') \prod_{\mathbf{k}' \in l'} \left[\sum_{\beta} U_{\beta 1}(\mathbf{k}' + \Delta\mathbf{k}') c_{\mathbf{k}'+\Delta\mathbf{k}'\beta\uparrow}^\dagger \right] |0\rangle. \end{aligned} \quad (\text{S14})$$

Considering small $|\theta - \theta'|$, because $\theta' = \theta + \Delta\theta$, $\langle 0 | c_{\mathbf{k}+\Delta\mathbf{k}\alpha\uparrow} c_{\mathbf{k}'+\Delta\mathbf{k}'\beta\uparrow}^\dagger | 0 \rangle$ is approximated to be $\delta_{\alpha\beta} \delta_{\mathbf{k}\mathbf{k}'}$. This leads to a simple expression

$$\langle \Phi(\theta) | \Phi(\theta') \rangle \approx \sum_l V_{1l}^*(\theta) V_{1l}(\theta') \prod_{\mathbf{k} \in l} \left[\sum_{\alpha} U_{\alpha 1}^*(\mathbf{k} + \Delta\mathbf{k}) U_{\alpha 1}(\mathbf{k} + \Delta\mathbf{k}') \right]. \quad (\text{S15})$$

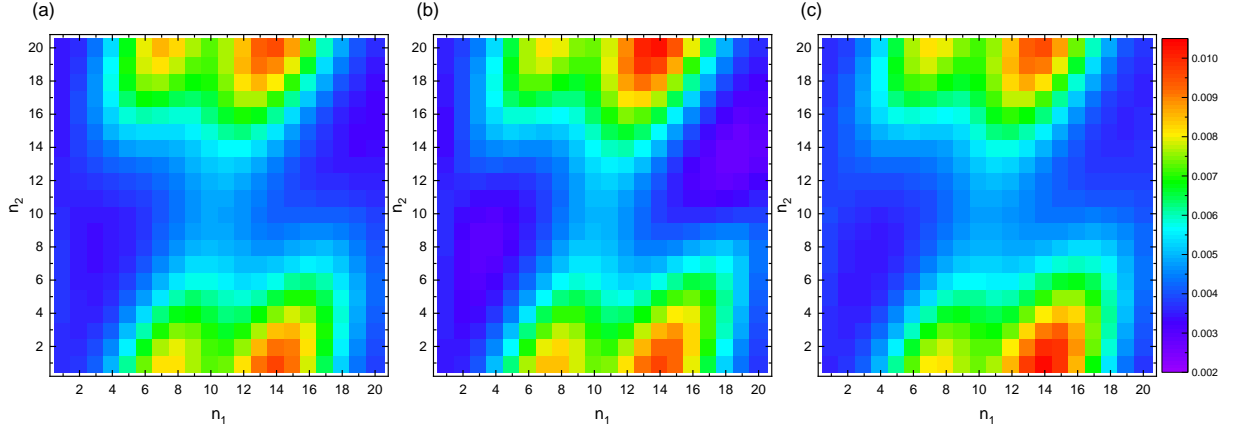


FIG. S8: Many-body Berry curvature as a function of discretized boundary phases for (a) sector $(k_1, k_2) = (0, 0)$, (b) sector $(0, 2)$, and (c) sector $(0, 4)$. Parameter values are $t_\delta = 0.5$, $r_2 = -0.2$, $\lambda = 0.2$ with $U = 2$ and $V = 1$.

This is used to compute products of two wave functions in Eq. (S10). For the integral over two boundary phases, we divide the boundary phase unit cell into 20×20 meshes, numerically evaluate the partial derivative of the many-body wave function on each placket using a technique proposed in Ref. [S4], and sum up all the quantities.

Figure S8 shows $F_{(k_1, k_2)}(\theta_1, \theta_2)$ in a discretized grid (n_1, n_2) for the ground state manifold with $t_\delta = 0.5$, $r_2 = -0.2$, $\lambda = 0.2$ with $U = 2$ and $V = 1$. Along the n_1 direction, these plots are periodic. Along the n_2 direction, plot (a) is continuously connected to plot (b), plot (b) is connected to plot (c), and plot (c) is connected back to plot (a). This also confirm the threefold ground state manifold, where inserting one flux quantum along the \mathbf{b}_2 direction shifts the sector $(k_1, k_2) = (0, 0)$ to $(0, 2)$, $(0, 2)$ to $(0, 4)$, and $(0, 4)$ to $(0, 0)$.

[S1] J. C. Slater and G. F. Koster, Phys. Rev. **94**, 1498 (1954).

[S2] D. J. Thouless, M. Kohmoto, M. P. Nightingale, and M. den Nijs, Phys. Rev. Lett. **49**, 405 (1982).

[S3] R. B. Lehoucq, D. C. Sorensen, and C. Yang, *ARPACK Users' Guide* (SIAM, Philadelphia, 1997).

[S4] T. Fukui, Y. Hatsugai, and H. Suzuki, J. Phys. Soc. Jpn. **74**, 1674 (2005).